Journal of General Virology (2015), **96**, 3131–3142 DOI 10.1099/jgv.0.000245

Visualization and quantification of simian immunodeficiency virus-infected cells using non-invasive molecular imaging

Jiasheng Song,[1] Zhengxin Cai,[1] Alexander G. White,[1] Tao Jin,[1] Xiaolei Wang,[1] Deepak Kadayakkara,[2] Carolyn J. Anderson,[1] Zandrea Ambrose[3] and Won-Bin Young[1]

Correspondence
Won-Bin Young
Email: youngw@upmc.edu

[1]Department of Radiology, University of Pittsburgh School of Medicine, Pittsburgh, Pennsylvania, USA

[2]Department of Oncology, Johns Hopkins School of Medicine, Baltimore, Maryland, USA

[3]Division of Infectious Diseases, Department of Medicine, University of Pittsburgh School of Medicine, Pittsburgh, Pennsylvania, USA

In vivo imaging can provide real-time information and three-dimensional (3D) non-invasive images of deep tissues and organs, including the brain, whilst allowing longitudinal observation of the same animals, thus eliminating potential variation between subjects. Current *in vivo* imaging technologies, such as magnetic resonance imaging (MRI), positron emission tomography-computed tomography (PET-CT) and bioluminescence imaging (BLI), can be used to pinpoint the spatial location of target cells, which is urgently needed for revealing human immunodeficiency virus (HIV) dissemination in real-time and HIV-1 reservoirs during suppressive antiretroviral therapy (ART). To demonstrate that *in vivo* imaging can be used to visualize and quantify simian immunodeficiency virus (SIV)-transduced cells, we genetically engineered SIV to carry different imaging reporters. Based on the expression of the reporter genes, we could visualize and quantify the SIV-transduced cells via vesicular stomatitis virus glycoprotein pseudotyping in a mouse model using BLI, PET-CT or MRI. We also engineered a chimeric EcoSIV for *in vivo* infection study. Our results demonstrated that BLI is sensitive enough to detect as few as five single cells transduced with virus, whilst PET-CT can provide 3D images of the spatial location of as few as 10 000 SIV-infected cells. We also demonstrated that MRI can provide images with high spatial resolution in a 3D anatomical context to distinguish a small population of SIV-transduced cells. The *in vivo* imaging platform described here can potentially serve as a powerful tool to visualize lentiviral infection, including when and where viraemia rebounds, and how reservoirs are formed and maintained during latency or suppressive ART.

Received 23 October 2014
Accepted 6 July 2015

INTRODUCTION

Since the beginning of the human immunodeficiency virus (HIV) epidemic, almost 70 million people have been infected with the HIV virus and ~35 million people have died of AIDS [United Nations Joint Programme on HIV/AIDS (UNAIDS), 2013]. Successes with antiretroviral therapy (ART) have greatly reduced the mortality caused by HIV infection and prolonged the lifespan of HIV-infected patients. However, persistence of the HIV genome even during effective ART leads to latent viral reservoirs, such as in the brain and lymphoid tissues (Eisele & Siliciano, 2012). This has been evidenced by rebound of viraemia in patients after withdrawal of ART that had successfully inhibited virus below the limit of detection in plasma (Chun *et al.*, 1999; García *et al.*, 1999; Harrigan *et al.*, 1999; Neumann *et al.*, 1999; Wong *et al.*, 1997). Traditional approaches such as a small biopsy or testing viral load in plasma are unable to reveal the temporal and spatial nature of HIV reservoirs, and thus *in vivo* monitoring of virus replication dynamics in real-time is urgently needed for studying HIV-1 persistence. In this study, we explored the use of *in vivo* imaging to visualize and quantify lentiviral dissemination and persistence without sacrificing animals, which should enable a longitudinal investigation of infection dynamics prior to and after ART.

Positron emission tomography-computed tomography (PET-CT) and magnetic resonance imaging (MRI) are non-invasive *in vivo* imaging techniques that are used routinely in clinical applications, either in a planar or three-dimensional (3D) format, with intricate resolution

One supplementary video and four supplementary figures are available with the online Supplementary Material.

and contrast (Cherry, 2006). These imaging approaches have also been used in basic research to image experimental animals, including non-human primates (Logothetis *et al.*, 1999; Nader *et al.*, 2006). Compared with PET-CT, MRI can provide higher spatial resolution at near-cellular level, but with much lower sensitivity (Lecchi *et al.*, 2007). Previous efforts using MRI in HIV research were mostly focused on imaging the pathogenesis caused by HIV or simian immunodeficiency virus (SIV) infection in the brain of patients or experimental non-human primates (Archibald *et al.*, 2004; Di Mascio *et al.*, 2009; Venneti *et al.*, 2008; Zhang & Li, 2013).

For basic research, bioluminescence imaging (BLI) offers an extremely high signal-to-background ratio, making the technique very sensitive. BLI can be easily applied to small animals; however, the limits of visible light penetration and tissue-associated light scattering precludes its use for studying deep tissues in larger animals (Choy *et al.*, 2003). To establish non-invasive multi-modality imaging platforms for tracking SIV-transduced cells *in vivo*, we generated a series of SIV reporter viruses that carried different imaging reporter genes and tested the feasibility of tracking virally infected cells in mouse models using the aforementioned imaging modalities.

RESULTS

Packaging capacity of SIV

SIV has been engineered by other groups to carry exogenous genes such as those for GFP (Alexander *et al.*, 1999b), HIV-1 Nef (Alexander *et al.*, 1997, 1999a), IL-2 (Gundlach *et al.*, 1997), firefly luciferase (Pöhlmann *et al.*, 1999) and IFN-γ (Giavedoni & Yilma, 1996) to investigate the dissemination of SIV *ex vivo* (Alexander *et al.*, 1999b; Pöhlmann *et al.*, 1999), chimeric SHIV (Alexander *et al.*, 1997) or for vaccine development (Giavedoni & Yilma, 1996). Thus far, the packaging capacity of SIV to include a reporter has not yet been characterized. We have systematically inserted reporter cassettes of different sizes into SIV_{mac239}-GFP and packaged the SIV reporter virus via DNA transfection in human embryonic kidney (HEK) 293 cells. For the accuracy of titre determination, the SIV reporter virus was pseudotyped with vesicular stomatitis virus glycoprotein (VSV-G) for titre assay on 293FT cells because 293FT cells are not susceptible to SIV infection, by which we could prevent the titre increase by possible SIV replication. Viral titre dramatically decreased by ninefold when the insert size in SIV_{mac239} increased from 2.2 (SIV_{mac239}-GFP-IRES-ΔSSTR2, 9.0×10^4 IU ml^{-1}) to 2.4 kb (SIV_{mac239}-GFP-T2A-Luc, 1×10^4 IU ml^{-1}) (Table 1, Fig. 1). No detectable viral titre was observed when the insert size increased to 2.8 kb (SIV_{mac239}-GFP-IRES-Luc), which indicated the maximum limit of packaging capacity. However, for optimal performance, the maximum size of an insert that does not significantly affect the infectious activity of SIV_{mac239} is 2.2 kb (Fig. 2). We also determined the replication kinetics of each reporter virus in CEMx174 cells without VSV-G pseudotyping at m.o.i. 0.1 over a period of at least 12 days via GFP expression and/or reverse transcriptase activity in the viral supernatants. The infectious activity of the SIV reporter viruses with insert size ≤ 2.2 kb was similar to that of WT SIV_{mac239} (Fig. 2).

Table 1. Packaging capability of replication-competent SIV reporter virus

See Fig. 1 and Methods for further details and abbreviations.

Constructs	Insert size (kb)	Viral titre (IU ml^{-1})*
SIV_{mac239}-GFP	0.7	1×10^5
SIV_{mac239}-GFP-IRES-Ft	1.8	1.2×10^5
SIV_{mac239}-GFP-T2A-SSTR2	1.9	8×10^4
SIV_{mac239}-GFP-IRES-ΔSSTR2†	2.2	9×10^4
SIV_{mac239}-GFP-T2A-Luc	2.4	1×10^4
SIV_{mac239}-GFP-IRES-Luc	2.8	<10
SIV_{mac239}-CMV-GFP-Luc	3.1	<10

*The titre of reporter viruses was based on GFP expression. IU, Infectious units.
†ΔSSTR2 had a deletion of 45 aa in the C terminus of somatostatin receptor type 2 (SSTR2).

BLI

As human colorectal carcinoma cell line HCT116 is not susceptible to SIV infection, SIV reporter virus was pseudotyped with VSV-G protein to transduce HCT116 cells. For *in vivo* imaging, 1×10^6 HCT116 cells transduced with VSV-G-pseudotyped SIV_{mac239}-eLuc were

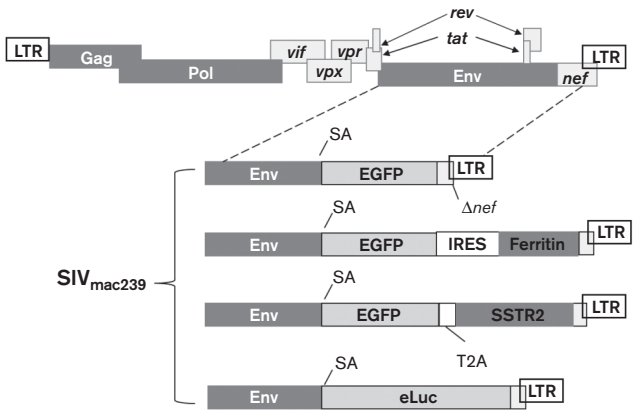

Fig. 1. Schematics of SIV_{mac239} reporter virus. Transcription of GFP (EGFP) and a reporter is driven by the 5′ LTR after the alternative splicing. SA, Splice acceptor. T2A (a small self-cleaving peptide from foot-and-mouth disease virus) or IRES (internal ribosomal entry site from picornavirus) is used for bicistronic expression of both GFP and the reporter. The genes or genetic elements depicted in this figure are not drawn to scale.

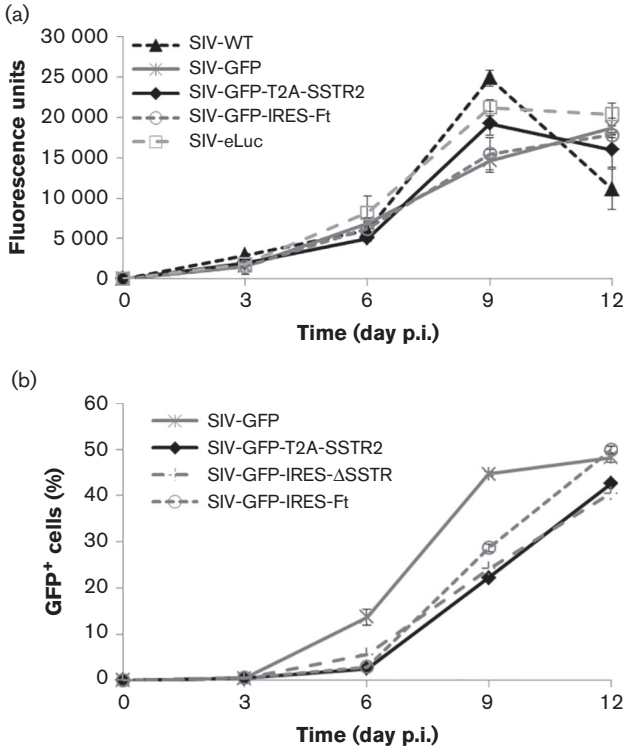

Fig. 2. Replication kinetics of reporter viruses and WT SIV_{mac239} in CEMx174 cells. (a) Replication kinetics was determined by measuring reverse transcriptase enzyme activity in the supernatants of infected cells. (b) Replication kinetics was determined using FACS on GFP expression of infected cells and expressed as the percentage of the total cell population.

transplanted in the left flanks of nude mice ($n=3$), whilst counterpart cells transduced with VSV-G-pseudotyped SIV_{mac239}-GFP were transplanted in the right flank. Whole-animal bioluminescence images were acquired on days 4, 11 and 16 post-transplantation. High-intensity bioluminescence was detected only from the HCT116 cells transduced with SIV_{mac239}-eLuc (left side), in which only 3.7 % of the cells were p27-positive by FACS analysis before transplantation; in contrast, bioluminescence was not observed from the cells transduced with SIV_{mac239}-GFP (Fig. 3a). The bioluminescence intensity was correlated with the increased numbers of cells transduced with SIV_{mac239}-eLuc over time (Fig. 3b).

To determine the sensitivity of *in vivo* BLI, a total volume of 100 µl Matrigel containing 5, 50, 500, 5000 or 11 700 HCT116 cells transduced with VSV-G-pseudotyped SIV_{mac239}-eLuc was transplanted at different locations as shown in Fig. 3(c) and imaged 36 h post-transplantation to allow the HCT116 cells to attach to the host tissues, which allowed the host tissues to provide the imaging substrates and tracers via blood circulation. However, the cell number should not increase significantly because the doubling time of HCT116 is ~20 h along with the consideration of possible cell death associated with transplantation. A discernible light signal was obtained with as few as five SIV_{mac239}-eLuc-transduced HCT116 cells, consistent with previously published results indicating <10 murine T-cells can be clearly visualized (Rabinovich *et al.*, 2008). The emission (total photon flux) was linearly correlated with the number of SIV-transduced HCT116 cells ($R^2=0.9$; Fig. 3d).

PET-CT imaging

PET imaging coupled with CT (PET-CT) (Antoch *et al.*, 2003), MRI or PET-MRI (Judenhofer *et al.*, 2008) are routinely used in the clinic for diagnostic purposes. To visualize and quantify SIV-transduced HCT116 cells in three dimensions using PET-CT, SIV constructs with human somatostatin receptor type 2 (hSSTR2) were engineered to become SIV_{mac239}-GFP-T2A-SSTR2. HCT116 cells were transduced with VSV-G-pseudotyped SIV_{mac239}-GFP-T2A-SSTR2 to express hSSTR2 for internalization and cell surface binding assays of ^{64}Cu-labelled CB-TE1A1P-Y3-TATE, a PET ligand to SSTR2, in comparison with HCT116 transduced with SIV_{mac239}-GFP (Fig. 4). The binding and internalization of the radiotracer could be blocked by Y3-TATE, indicating uptake specificity (Fig. 4c). The expression of SSTR2 in transduced HCT116 was confirmed by Western blot analysis (Fig. 4d).

For *in vivo* imaging, 1×10^6 HCT116 cells transduced with SIV_{mac239}-GFP-T2A-SSTR2 by VSV-G pseudotyping (9 % of cells expressing GFP and therefore SSTR2) were implanted in the left flanks of nude mice ($n=4$). As a negative control, HCT116 cells transduced with SIV_{mac239}-GFP (57 % of cells with GFP expression) were transplanted in the right flanks of the same mice. PET images were acquired 11 days after transplantation and demonstrated that the tumours derived from HCT116 transduced with SIV_{mac239}-GFP-T2A-SSTR2 showed uptake of [^{64}Cu]CB-TE1A1P-Y3-TATE, but not the cells transduced with SIV_{mac239}-GFP (Fig. 5a). The standard uptake value (SUV), a semiquantitative measurement for diagnostic PET-CT imaging (Velikyan *et al.*, 2014), was used to normalize the tracer uptake in SIV-infected cells versus control cells *in vivo*. The SUV of HCT116 transduced with SIV_{mac239}-GFP-T2A-SSTR2 was 1.0 compared with 0.1 measured in the control group. This 10-fold difference indicated high specific uptake of radiotracer by SSTR2-expressing cells (*t*-test, $P<0.0001$) (Fig. 5b). Only minimal radiotracer was detected in the non-targeted tissues, with the exception of the kidneys and bladder due to the renal clearance excretion pathway (Guo *et al.*, 2012). Due to an extremely low uptake in muscle, the target-to-muscle ratio was relatively high in SSTR2-expressing tumours (70 ± 32-fold; $n=4$) without any significant background observed (high signal-to-noise ratio).

The advantage of using PET-CT imaging is its high sensitivity, high resolution, quantification and unlimited penetration, which allows for monitoring of the temporal and spatial locations of SIV-infected cells deep inside

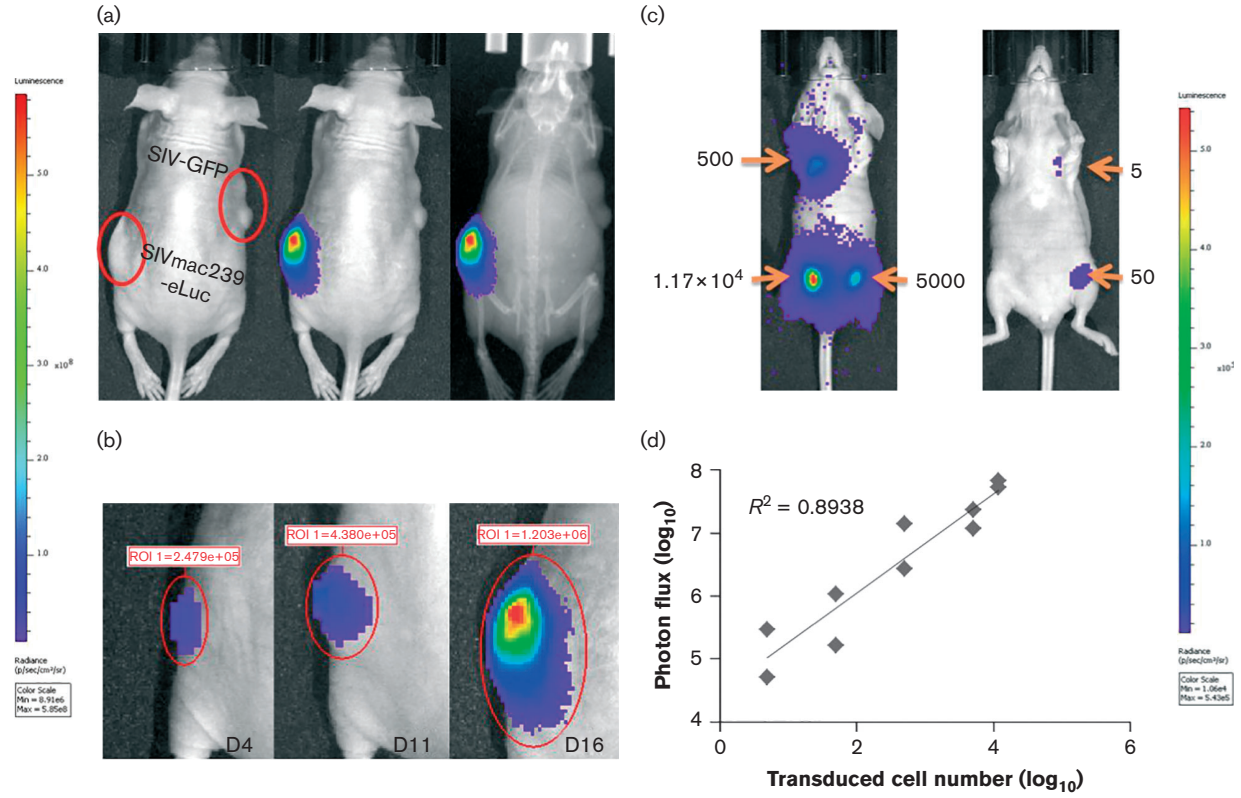

Fig. 3. *In vivo* imaging of SIV_{mac239}-eLuc-infected cells based on eLuc. (a) BLI was performed on day 11 post-transplantation and overlaid onto a photographic or X-ray image to visualize the transplanted HCT116 cells transduced with SIV_{mac239}-eLuc. (b) The progression of tumours in the same mice was monitored in real-time by BLI. (c) In total, 5 single cells to 1.1×10^4 cells infected with SIV_{mac239}-eLuc were transplanted subcutaneously in mice and imaged by BLI 36 h post-transplantation. (d) The number of SIV_{mac239}-eLuc-transduced cells was plotted against total photon flux emission.

organs or tissues with an intricate 3D anatomical context (Video S1, available in the online Supplementary Material). To determine the detection sensitivity, HCT116 cells (1×10^2, 1×10^3, 1×10^4 or 3.9×10^4) transduced with SIV_{mac239}-GFP-T2A-SSTR2 were transplanted in the upper body to avoid interference from the kidneys. The efficacy of transduction prior to cellular transplantation was analysed by FACS for both GFP and p27 expression (Fig. S1). A cell population of as few as 10 000 SIV_{mac239}-GFP-T2A-SSTR2-transduced cells could be imaged at 36 h post-transplantation (Fig. 5c).

MRI imaging

Ferritin is a cellular protein that can form a polymer cage used for storing intracellular iron in a non-toxic form and is responsible for the physiological homeostasis of iron metabolism. Due to its crystalline ferrihydrite core, ferritin exhibits an anomalously high superparamagnetism (Bulte *et al.*, 1994) and a marked effect on water NMR relaxation rates (Bulte *et al.*, 1994; Gottesfeld & Neeman, 1996; Vymazal *et al.*, 1996, 1998). Gene expression of ferritin can increase magnetic contrast, and can be visualized and quantified by MRI. To perform MRI on infected cells, 293FT cells transduced with either SIV_{mac239}-GFP-IRES-Ft or SIV_{mac239}-GFP via VSV-G pseudotyping were measured for T_2* and imaged in a 9.4 T Varian magnetic resonance scanner 3 days after transduction (Fig. 6a). Based on FACS analysis for GFP expression, only 6 % of the cells were transduced with SIV_{mac239}-GFP-IRES-Ft, whilst 7 % of cells were transduced with SIV_{mac239}-GFP (Fig. S2). However, despite a small ferritin-expressing population, the increase in magnetic contrast represented as a T_2* value is distinguishable from the negative control, 17.5 versus 19.8 ms. T_2 was also measured as it seemed more robust than T_2*, with results of 21.0 versus 23.7 ms. The increased magnetic contrast was illustrated in a T_2* map (Fig. 6a). The expression level of ferritin was further confirmed by Western blot analysis (Fig. 6b).

For *in vivo* imaging of MRI, nude mice were transplanted with 1×10^6 HCT116 cells transduced with VSV-G-pseudotyped SIV_{mac239}-GFP-IRES-Ft (10 % GFP^+ cells) or SIV_{mac239}-GFP (57 % GFP^+ cells) (n=3), in which only two mice developed tumours and were perfused with 4 % paraformaldehyde (PFA) on day 16 post-transplantation for MRI. Scout images of the anatomical details were first

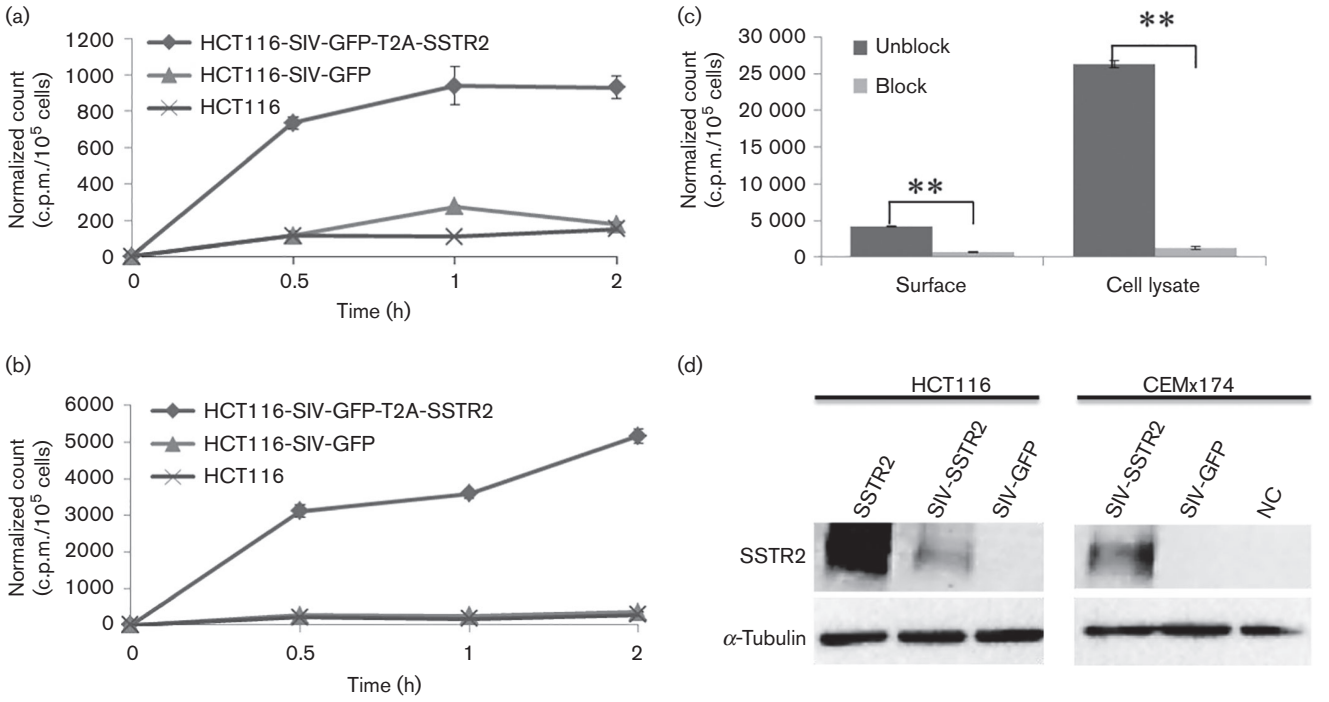

Fig. 4. Cell surface binding and internalization of radiotracer [^{64}Cu]CB-TE1A1P-Y3-TATE by SIV-transduced cells. (a) Cell surface binding and (b) internalization of radiotracer in HCT116 cells and HCT116 cells transduced with SIV_{mac239}-GFP-T2A-SSTR2 or SIV_{mac239}-GFP; $n=2$ for each data point; bar, SD. Note that 9 % of cells were transduced with SIV_{mac239}-GFP-T2A-SSTR2 and 57 % of cells were transduced with SIV_{mac239}-GFP based on GFP expression by FACS. (c) Blocking of SSTR2 in HCT116 cells transduced with SIV_{mac239}-GFP-T2A-SSTR2 by incubating with 2 μg octerotide for 2 h to demonstrate the uptake specificity of radiotracer was analysed on cell surface binding (surface) and internalization (cell lysate). (d) Western blotting of HCT116 and CEMx174 cells transduced with SIV_{mac239}-GFP-T2A-SSTR2 and SIV_{mac239}-GFP was performed using antibodies against SSTR2 and α-tubulin. HCT116 cells stably expressing SSTR2 previously established by transfection were used as a positive control (SSTR2) and non-expressing HCT116 were used as a negative control (NC).

used to determine the positions of the tumours before measuring the magnetic contrast (Fig. S3). As iron increases the water transverse relaxation rate, the magnetic contrast could be distinguished using a map of relaxation ($R_2=1/T_2$) displayed using a colorimetric scale, where yellow pixels indicated high R_2 values (Fig. 6c). The mean R_2 values measured in the ferritin-expressing tumours and the control tumours in Mouse 1 and Mouse 2 were 36.0 ± 1.8 versus 37.2 ± 1.8 and 37.9 ± 1.9 versus $39.0\pm1.6\ s^{-1}$, respectively. The increase in the R_2 due to ferritin was 5 %, which was distinguishable from the negative control using MRI.

In vivo visualization of EcoSIV infection

Without using an expensive non-human primate model to demonstrate the proof-of-concept that *in vivo* imaging can be used to visualize viral infection, an EcoSIV based on the aforementioned SIV_{mac239}-eLuc was constructed by replacing the SIV gp120 gene with the gp80 gene from ecotropic murine leukemia virus (MLV). The entry of EcoSIV is based on the receptor used by MLV, i.e. the cationic amino acid transporter-1. This approach has been previously established for converting the infectious tropism of HIV from humans to rodents (Potash *et al.*, 2005). Four male nude mice were inoculated with $EcoSIV_{mac239}$-eLuc via intraperitoneal injection for longitudinal monitoring of viral activity via BLI. Bioluminescence images were acquired using an IVIS Lumina XR system on days 1, 3 and 7 post-infection (p.i.) without observing any notable EcoSIV infection. At 12 days p.i., evidence of viral infection through bioluminescence signal in the gut region of the mice was visualized. Continued monitoring was performed on days 17 and 25 days p.i. (Fig. 7b–d). Following imaging on day 25, mice were euthanized and imaged with skin removed to show localized bioluminescence from *in vivo* infected cells (Fig. 7e). Tissues with noted bioluminescence from imaging were harvested for DNA and RNA extraction. SIV proviral DNA was amplified from cellular genomic DNA using nested PCR, validated by *Kpn*I digestion and then sequencing (Fig. S4A, B). Reverse transcription (RT)-PCR was used to demonstrate the SIV *gag* transcripts from the isolated intestine tissues (Fig. S4C).

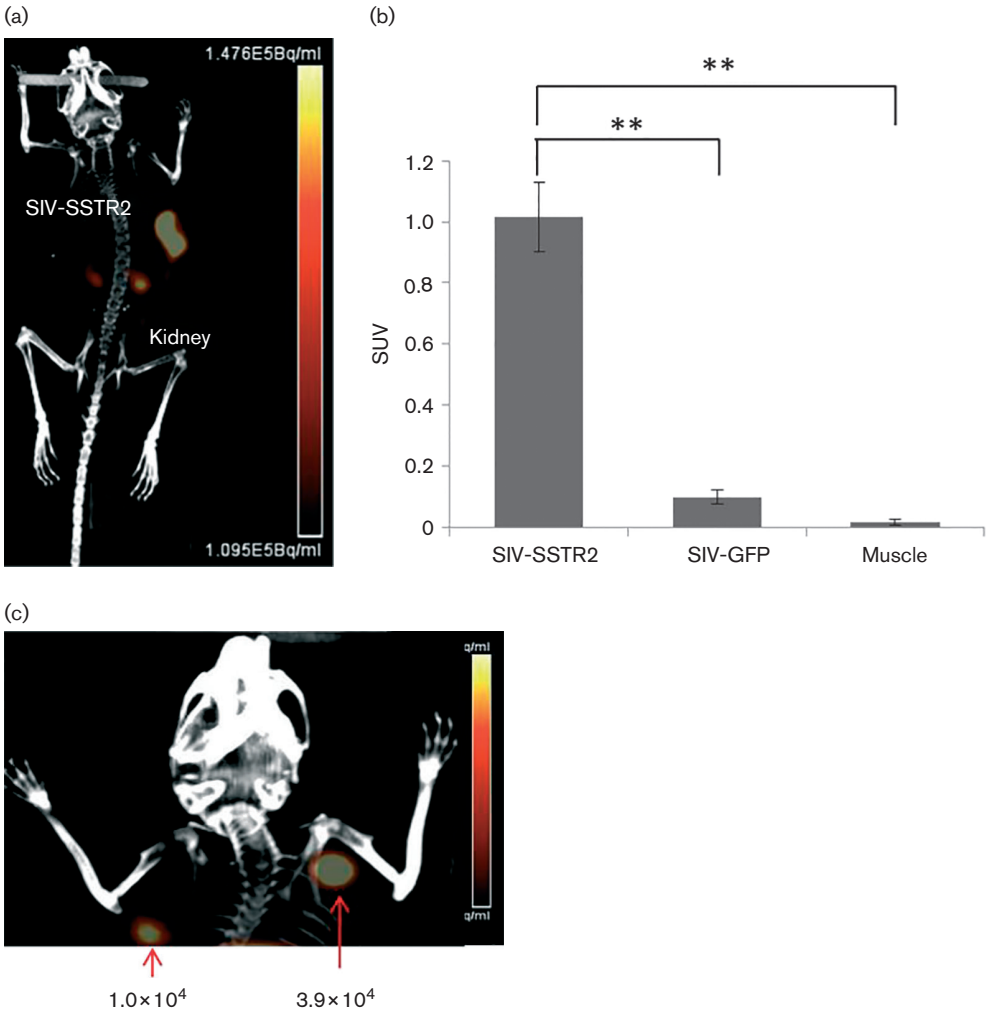

Fig. 5. PET-CT imaging of HCT116 cells transduced with SIV_{mac239}-GFP-T2A-SSTR2 *in vivo*. (a) A PET-CT image of a representative mouse transplanted with HCT116 cells transduced with SIV_{mac239}-GFP-T2A-SSTR2 11 days post-transplantation. (b) Standard uptake values (SUVs) were calculated by measuring regions of interest (ROI) from each PET-CT image and compared amongst tumours transduced with SIV_{mac239}-GFP or SIV_{mac239}-GFP-T2A-SSTR2 to muscle. Results are reported as mean ± SD; $n=4$; $^{**}P<0.0001$. (c) In total, 1×10^2 to 3.9×10^4 HCT116 cells transduced with SIV_{mac239}-GFP-T2A-SSTR2 were transplanted subcutaneously in nude mice and imaged by PET-CT scanning 36 h post-transplantation (only the image of 1.0×10^4 and 3.9×10^4 transplanted cells is shown).

The entire infected cell population was reduced from day 12 to 17 as shown by regions of interest (ROI) analysis of the total photon flux emission from the whole animal, and the head, chest and abdomen regions (Fig. 7f). The bioluminescence signal remained at similar levels between days 17 to 25, indicating a levelling off of cell infection. The biodistribution of the entire infected cell population was constant among the head, upper and lower bodies in the entire imaging session from days 12 to 25 p.i., which was determined by the percentage of infected cell population from each major portion of the body over the total infected cell population quantified from the whole body (Fig. 7g).

DISCUSSION

As lentiviral infection involves multiple organs and tissues, and is complicated by multicellular interactions, studying pathogenesis in a whole animal would be meaningful and could provide important information of reservoir formation and maintenance. However, to perform needle-point biopsy on all infected tissues in a large experimental animal, such as a non-human primate, is simply impossible. *In vivo* imaging, however, is non-invasive, and provides a rapid assessment of the extent and 3D distribution of target cells in a manner that is not feasible using invasive procedures such as biopsies or necropsies for microscopic examination.

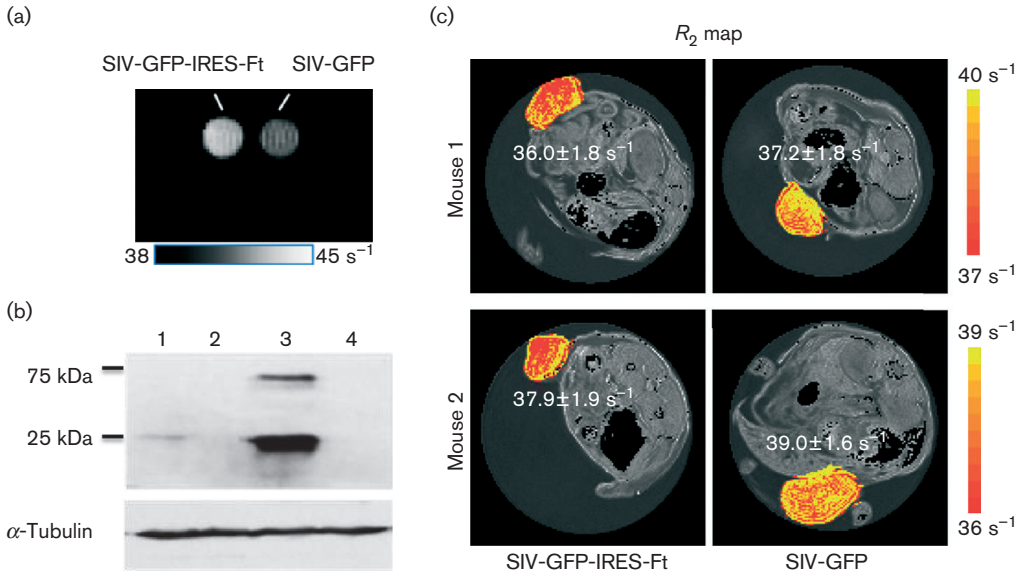

Fig. 6. Magnetic contrast by ferritin expression in infected cells *in vitro* and *in vivo*. (a) Increased contrast measured by a 9.4 T Varian magnetic resonance scanner in cell pellets of 1×10^6 293FT cells transduced with SIV_{mac239}-GFP-IRES-Ft (5.5 % infected population) or SIV_{mac239}-GFP (7.1 % infected population). (b) Western blot of 293FT and CEMx174 cells infected with SIV_{mac239}-GFP-IRES-Ft (lane 1 and 3, respectively) or infected with SIV_{mac239}-GFP (lanes 2 and 4, respectively) using antibodies against human ferritin. (c) Two nude mice transplanted with HCT116 cells transduced with SIV_{mac239}-GFP-IRES-Ft were imaged by MRI on day 16 post-transplantation. The R_2 values are displayed in a colour scale where yellow pixels indicate high R_2 values with the mean R_2 values shown next to tumours.

One of the most important questions in engineering a reporter HIV or SIV for *in vivo* imaging of infection is whether the engineered virus has a phenotype and replication capacity similar to the WT virus. In this study, we inserted reporter cassettes of various sizes into an SIV and demonstrated that the maximum insert in a SIV is 2.2–2.4 kb. The exogenous reporter genes engineered in SIV were expressed via an alternative splicing signal used for the *nef* transcript according to previous studies (Alexander *et al.*, 1997; Giavedoni & Yilma, 1996; Gundlach *et al.*, 1997; Pöhlmann *et al.*, 1999). Without the expression of Nef, the reporter SIV in this study can still retain infectious activity similar to the WT, because deletion of *nef* posts a minimal effect on SIV replication in many cell types (Gibbs *et al.*, 1994). SIVs deficient in Nef were also demonstrated to be infectious in monkeys (Alexander *et al.*, 1999b; Hofmann-Lehmann *et al.*, 2003). Nef has been shown to be important for SIV pathogenesis in rhesus macaques (Johnson & Desrosiers, 2002; Kestier *et al.*, 1991; Sawai *et al.*, 1996).

BLI is an affordable imaging modality with high sensitivity and specificity (Edinger *et al.*, 2002). The shortcoming of using BLI is the limit of penetration depth to $\sim$1 cm, which makes it practical for only small-animal imaging (Choy *et al.*, 2003; Dothager *et al.*, 2009). Using an enhanced firefly luciferase (eLuc) (Rabinovich *et al.*, 2008), we can visualize as few as five HCT116 cells transduced with VSV-G-pseudotyped SIV_{mac239}-eLuc (Fig. 4c). The photon flux was linearly correlated with numbers of SIV_{mac239}-eLuc-transduced cells (Fig. 4d). Based on these findings, establishing a non-invasive BLI for HIV-1 infection in small animals, such as humanized mice, would be useful for evaluating the effectiveness of antiviral regimes, identifying anatomical and pharmacological sanctuaries in association with persistent HIV-1 replication (Fletcher *et al.*, 2014), and isolating drug-resistant variants (Nischang *et al.*, 2012).

To quantify SIV/SHIV infection non-invasively in non-human primates, PET-CT imaging used in clinics may be the most promising tool because it provides 3D images with very high sensitivity. In this study, hSSTR2 was chosen as the reporter over others such as the sodium iodide symporter (Chung, 2002), herpes simplex virus 1 thymidine kinase (Gambhir *et al.*, 2003) and CB_2R (Evens & Bormans, 2010) because the radiolabelled ligand [^{64}Cu]CB-TE1A1P-Y3-TATE has high binding affinity to SSTR2 ($K_d = 1.8 \pm 0.5$ nM), and a favourable pharmacokinetics with fast targeting and rapid blood clearance resulting in relatively low background (Guo *et al.*, 2012). SSTR2 is also expressed at much lower levels in certain tissues, pituitary gland, pancreas and adrenals (Patel, 1999), which does not significantly interfere with imaging viral infection (Fig. 6). This study has shown that PET imaging based on SSTR2 can detect as few as 10^4 infected cells (Fig. 6c). With unlimited penetration by positron particles, highly favourable

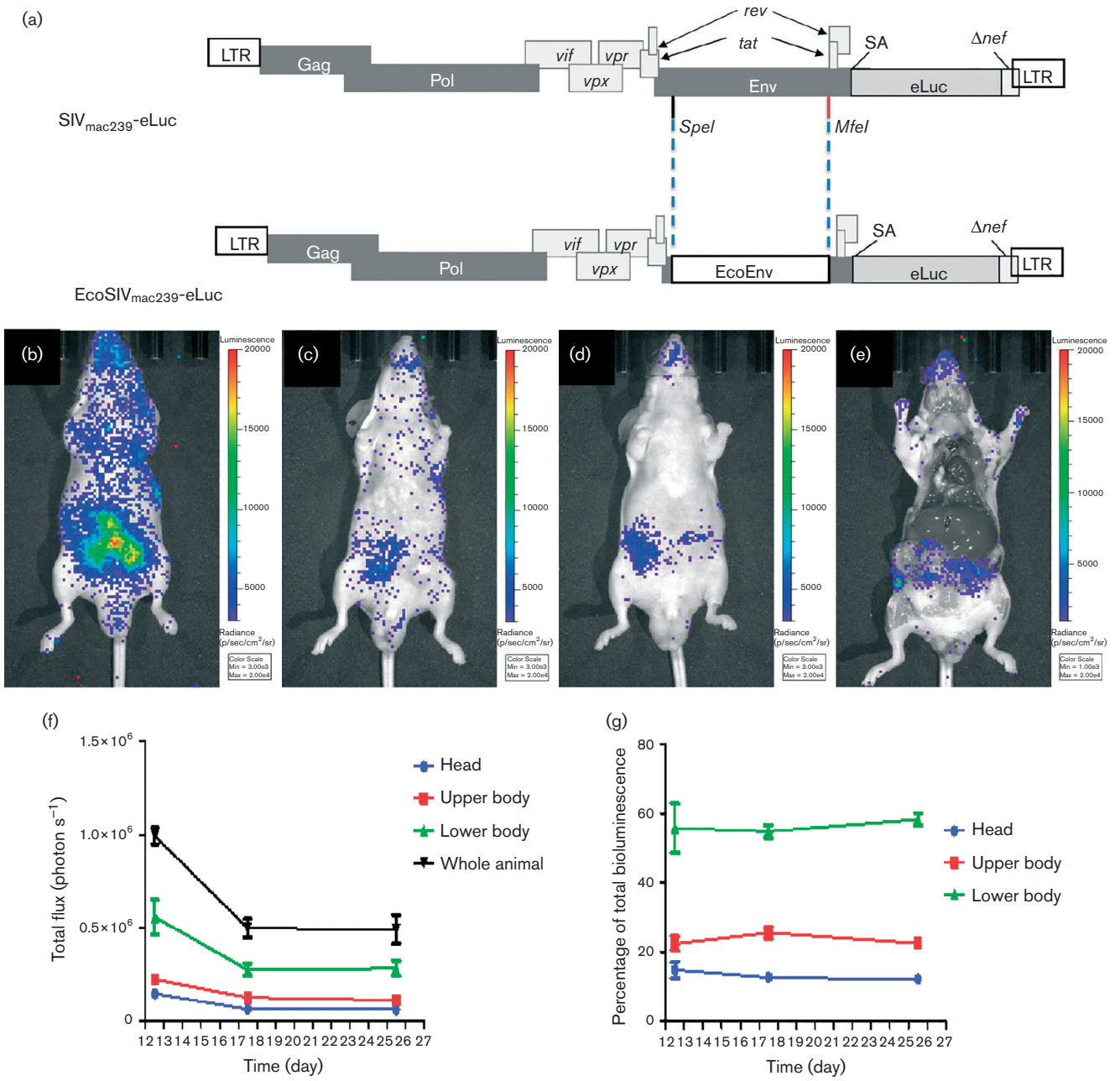

Fig. 7. Visualization of EcoSIV infection *in vivo*. (a) EcoSIV$_{mac239}$-eLuc was engineered with the envelope from ecotropic MLV in the position of SIV gp120.SA, splice acceptor. (b–d) Mice were inoculated with EcoSIV carrying eLuc (EcoSIV$_{mac239}$-eLuc) via intraperitoneal injection, and imaged at 12 (b), 17 (c) and 25 days p.i. (d). (e) Following imaging on day 25, mice were euthanized and the organs were exposed to show localized bioluminescence from infected cells. Images are scaled equally in radiance units (see Methods); $n=4$. (f) Total flux of radiance from each portion of the body was plotted against the time points p.i. to illustrate the dynamics of infected cells in each portion of the body and the whole body over time. (g) The biodistribution of infected cells in each portion of the body was constant over time.

pharmacokinetics and high sensitivity, this PET-CT imaging system can be used for monitoring the dynamics of SIV infection to uncover virus reservoirs and evaluate the effectiveness of antiviral regimens, therapies or vaccines in non-human primates longitudinally.

An inherent limit to PET-CT imaging using peptides and antibodies as imaging agents is the penetration capacity into the blood–brain barrier. In contrast, *in vivo* MRI of gene expression in this study is based on the use of ferritin as a magnetic contrast agent to monitor transferred gene

expression without the need for exogenous tracers or probes (Cohen *et al.*, 2005; Deans *et al.*, 2006; Genove *et al.*, 2005; Iordanova & Ahrens, 2012). Ferritin is primarily responsible for the storage of intracellular iron in a non-toxic form, and is a natural source of intrinsic MRI contrast in various tissues and organs (Genove *et al.*, 2005). The level of ferritin and its iron content can be quantified by MRI, which has been widely used clinically to measure tissue iron in the human brain (Kirsch *et al.*, 2009; Pfefferbaum *et al.*, 2009; Yao *et al.*, 2009), liver (Beaumont *et al.*, 2009) and heart (Guo *et al.*, 2009). Compared with PET imaging, MRI can provide a much higher spatial resolution, but at the sacrifice of lower sensitivity. The increase of R_2 value, even by only 5 %, in tumours transduced with SIV_{mac239}-GFP-IRES-Ft, can be distinguished by high-field MRI as demonstrated in this study, because these values were obtained from five repeats at each of 12 different time points for statistical significance – a task that cannot be achieved with other imaging modalities. Imaging the pathogenesis in the brain caused by lentiviral infection as well as tracking the infected locations in the same MRI session would be a very attractive approach to correlate the location of infected cells with their pathogenesis for a better understanding of HIV-associated dementia (Aylward *et al.*, 1995; Ernst *et al.*, 2002; McArthur, 2004).

METHODS

Plasmid constructs. SIV_{mac239} was obtained from the National Institutes of Health (NIH) AIDS Reagent Program and SIV_{mac239}-GFP was originated from Dr Louis Alexander (Alexander *et al.*, 1999b). An internal ribosomal entry site (IRES) was inserted into SIV_{mac239}-GFP to construct the first-generation reporter SIV for the bicistronic expression of both GFP and ferritin, an MRI contrast agent, to become SIV_{mac239}-GFP-IRES-Ft. The cassette IRES-Ft (Ft, human heavy chain ferritin) was amplified by using PCR primers designed with *Sac*II digestion sites at the 5′ and 3′ ends of the primers for cloning into *Sac*II-digested SIV_{mac239}-GFP, in which *Sac*II digestion site was previously inserted at the 3′ end of GFP in SIV_{mac239}-GFP (Alexander *et al.*, 1999b).

Other constructs were generated using a similar approach (Fig. 1, Table 1). The full-length PET imaging reporter gene hSSTR2 was amplified from pCR2.1-TOPO-SSTR2 (kindly provided by Dr Stephen Thorne, University of Pittsburgh, USA). The eLuc gene was amplified from pRV2011-OFL (kindly provided by Dr Hyam Levitsky, Johns Hopkins University, USA). To reduce the size of the reporter cassette, a self-cleaving 2A peptide from *Thosea asigna* virus (T2A, 54 bp) was used in place of an IRES sequence for bicistronic expression of both GFP and hSSTR2 to produce SIV_{mac239}-GFP-T2A-SSTR2, the second-generation reporter SIV (Fig. 1). Owing to the large size of eLuc (1.6 kb), we also inserted only the eLuc gene in place of GFP to create SIV_{mac239}-eLuc.

Construction of $EcoSIV_{mac239}$-eLuc was based on the aforementioned SIV_{mac239}-eLuc. The gp80 of MLV was PCR amplified from the pHCMV-EcoEnv41 requested from Addgene (plasmid 15802) and then cloned in-frame into the *Spe*I and *Mfe*I restriction sites located in SIV gp120 as indicated in Fig. 7(a).

PCR and RT-PCR. Genomic DNA was extracted from the identified tissues after *in vivo* imaging using proteinase K digestion on minced samples followed by conventional phenol/chloroform extraction. PCR was perform using *gag*-specific primers ATAGTTTCTGTTGTTCCTGTTTCCACCA and CACCGAGGCTGGCAGATTGAGCCC. To ensure the right PCR product for *Kpn*I digestion and sequencing, nested PCR was performed using the primer set CACCGAGGCTGGCAGATTGAGCCC and TTCTTTCCGTTGGGTCGTAGCCT. RNA was extracted from the same tissues using TRIzol reagent (Invitrogen). First-strand cDNAs were synthesized with the aforementioned *gag*-specific primer ATAGTTTCTGTTGTTCCTGTTTCCACCA using Superscript III reverse transcriptase (Invitrogen). RT-PCR was performed using the aforementioned primer set for nested PCR on proviral DNA amplification.

Cell culture and *in vivo* transplantation. GHOST(3) X4/R5 cells (requested from the NIH AIDS Reagent Program), 293FT cells (Invitrogen) and HCT116 (human colorectal carcinoma cells; ATCC, CCL-247) were cultured in Dulbecco's modified Eagle's medium (DMEM) supplemented with 10 % FBS. CEMx174 cells were cultured in minimum essential medium (MEM) supplemented with 10 % FBS, penicillin and streptomycin (100 U ml^{-1}), and glutamine (2 mM). For *in vivo* transplantation, HCT116 cells were first transduced with VSV-G-pseudotyped SIV reporter virus for at least 3 days, and then trypsinized and resuspended in Matrigel in a volume of total 100 µl for subcutaneous injection.

Viral production and titre assay. To produce VSV-G-pseudotyped reporter SIVs for transducing human colorectal carcinoma cell line HCT116, 293FT cells were plated in PureCoat 24-well plates (BD) and transfected with 1 µg each SIV plasmid construct and 0.5 µg plasmid encoding VSV-G using Lipofectamine LTX reagent (Invitrogen). The titre of each aforementioned VSV-G-pseudotyped SIV reporter virus containing the GFP reporter was determined on 293FT cells and analysed for GFP expression (Table 1). Without the GFP reporter in the SIV_{mac239}-eLuc viral construct, GHOST(3) X4/R5 cells were used to determine the titre without VSV-G pseudotyping. For determining the replication kinetics of each SIV reporter virus on SIV-susceptible CEMx174 cells, supernatants containing reporter SIV without VSV-G pseudotyping were harvested from 293FT cells 48 h post-transfection and filtered through a 0.45 µm pore size sterile filter.

***in vitro* viral replication kinetics.** CEMx174 cells (1×10^5 cells) were placed in 15 ml conical tubes containing 1 ml MEM with 10 % FBS and inoculated with virus without VSV-G pseudotyping at m.o.i. 0.1 for 1 h at 37 °C. Cells were cultured in T25 flasks containing 7 ml medium at 37 °C with 5 % CO_2 and split at 1 : 2.5 every 3 days. The infected cells and supernatant at each time point were then separated by centrifugation for measuring replication kinetics *in vitro* based on the expression of three genes: GFP, HIV-1 reverse transcriptase or eLuc. Reverse transcriptase activity in collected supernatants was determined using the EnzCheck Reverse Transcriptase Assay kit (Invitrogen). eLuc activity in cell lysates was determined using the Luciferase Assay System (Promega) according to the manufacturer's instructions.

Internalization assay of radiolabelled tracer for SSTR2. As HCT116 is not susceptible to SIV infection, VSV-G pseudotyping was used to transduce HCT116 cells with SIV_{mac239}-GFP-T2A-SSTR2 for the internalization assay. In total, 2×10^5 SIV_{mac239}-GFP-T2A-SSTR2- or SIV_{mac239}-GFP-transduced HCT116 cells were plated in 24-well plates overnight and then washed twice with 0.5 ml Hank's balanced salt solution (HBSS). A aliquot of 0.5 ml DMEM with 10 % FBS was added to each well and then incubated at 37 °C with 5 % CO_2 for 10 min. For the blocking assay, Y3-TATE was added to each well before the tested cells were plated (Guo *et al.*, 2012). The tracer for PET, [^{64}Cu]CB-TE1A1P-Y3-TATE (0.5 mCi $nmol^{-1}$), was added to each well, and the cells were incubated at 37 °C with 5 % CO_2 for 30, 60 and 120 min. At each time point, radioactive media was removed and cells were washed with ice-cold HBSS to prevent further

internalization. To collect the surface-bound fraction, each well was treated with 1 ml 20 mM sodium acetate/HBSS (pH 4.0) at 37 °C for 10 min followed by a second wash without incubation. Both washes were pooled together for measuring cell surface binding of the tracer. After removal of the surface-bound fraction, the cells in each well were lysed with 1 ml 0.5 % SDS for an internalization assay. The internalized and surface-bound fractions were measured using a WIZARD Gamma Counter (Perkin Elmer) and normalized to c.p.m./10^5 cells.

Western blot analysis. Cells were lysed in RIPA buffer containing a protease inhibitor cocktail (Thermo Scientific). Proteins were separated electrophoretically on 12 % SDS-PAGE and transferred to PVDF membranes (Bio-Rad). The membranes were blocked for 1 h at room temperature with 5 % non-fat milk and then incubated for 1 h at room temperature with primary antibodies: anti-SSTR2 rabbit mAb (Abcam), anti-V5 mouse mAb (Invitrogen) or anti-tubulin rabbit mAb (Cell Signalling). The membrane was washed three times in PBS with 0.05 % Tween 20 and incubated with either anti-mouse or anti-rabbit mAbs conjugated with HRP (Cell Signalling).

BLI. All animal care and procedures were approved by the University of Pittsburgh Institutional Advisory Committee of Animal Care. Mice were anaesthetized via isoflurane inhalation and then injected intraperitoneally with D-luciferin potassium salt (150 mg kg^{-1}; Gold BioTechnology) dissolved in Dulbecco's PBS. Bioluminescence images were obtained using an IVIS Lumina XR (Perkin Elmer) and analysed with Living Image software (version 4.3.1; Caliper Life Sciences). For *in vivo* imaging of EcoSIV infection, ventral luminescence images were acquired for 5 min [open light filter, binning 8 × 8, f/stop 1, field of view (FOV) = 100 mm]. Image analysis and TIFF export were performed using Living Image. Images were scaled equally in radiance units (photons s^{-1} cm^{-2} sr^{-1}). To determine the biodistribution of infected cells, the total photon flux from each portion of the body (head, and upper and lower body) was converted to a percentage by dividing to the total photon flux from the whole body.

Small-animal PET-CT imaging. Small-animal PET-CT imaging was performed as described previously (Sprague *et al.*, 2004). Briefly, [^{64}Cu]CB-TE1A1P-Y3-TATE (3.7 MBq) was injected via the tail vein 2 h prior to imaging. PET images were taken in 3D mode followed by CT scanning in an Inveon PET-CT scanner (Siemens Medical Solutions) dedicated for small-animal imaging (Kemp *et al.*, 2009). Inveon Research Workplace (Siemens Healthcare Global) was used for co-registration of PET-CT images and quantification of ROI. PET-CT images were reconstructed with MAP (maximum a posteriori, followed by 3D OSEM (ordered-subset expectation maximization) and 2DFBP (filtered back projection) for presentation and quantifications, respectively. Standard uptake values (SUVs) were calculated by measuring ROI from each PET-CT image using the formula: SUV = (nCi ml^{-1}) × [animal weight (g)/injected dose (nCi)].

MRI. All MRI experiments were performed on a 9.4 T magnet equipped with an actively shielded 12 cm gradient system (Magnex) interfaced to a DirectDrive 2 console (Agilent). A total of 10^7 293FT cells transduced with VSV-G-pseudotyped SIV_{mac239}-GFP-IRES-Ft or SIV_{mac239}-GFP were pelleted by centrifugation at 224 *g*. The supernatant was removed and the cells were resuspended in 1 ml 4 % PFA. The cell pellets were scanned in a 9.4 T Varian magnetic resonance scanner using gradient-echo echo planar imaging (EPI) to measure T_2* and spin-echo EPI to measure T_2, echo time (TE) = 9–36 ms with 3 ms steps.

To scan the nude mice transplanted with HCT116 transduced with VSV-G-pseudotyped reporter SIV, the mice were sacrificed by perfusion with 4 % PFA and scanned with a 3.8 cm internal diameter quadrature volume coil (Rapid Biomedical). To measure the magnetic contrast, multi-echo fast spin-echo images were acquired on two slices, covering either the transplanted HCT116 expressing ferritin or the counterpart (Fig. 6). The imaging parameters were: FOV 30 mm × 30 mm, matrix size 128 × 128, slice thickness 1 mm, echo train length 8, repetition time (TR) = 2 s, 11 TE values from 30 to 50 ms in 2 ms steps and number of excitation (NEX) = 5. Water transverse relaxation rate (R_2) maps were calculated from a pixel-wise fitting of the image intensity to a mono-exponential decay function with respect to TE, as $S = S_0\exp(-R_2 \cdot TE)$. For quantitative analysis, the R_2 values were averaged for all pixels of the xenografted tumours and presented as mean ± SD.

Statistical analysis. Data are expressed as mean ± SD. Statistical significance was determined using the unpaired Student's *t*-test with two-tailed analysis (GraphPad); $*P < 0.05$, $**P < 0.01$.

ACKNOWLEDGEMENTS

This project is supported by a grant from the NIH/National Institute of Mental Health (1R21MH100949) to W.-B. Y. BLI and PET-CT were performed in the *In Vivo* Imaging Facility at the University of Pittsburgh Cancer Institute (UPCI), University of Pittsburgh School of Medicine, which is supported in part by grant P30CA047904 to the UPCI. We also would like to thank Ms Kathryn Day for assistance in BLI and PET-CT, and people in the Division of Laboratory Animal Resources at the University of Pittsburgh for animal care.

REFERENCES

Alexander, L., Du, Z., Rosenzweig, M., Jung, J. U. & Desrosiers, R. C. (1997). A role for natural simian immunodeficiency virus and human immunodeficiency virus type 1 nef alleles in lymphocyte activation. *J Virol* **71**, 6094–6099.

Alexander, L., Du, Z., Howe, A. Y., Czajak, S. & Desrosiers, R. C. (1999a). Induction of AIDS in rhesus monkeys by a recombinant simian immunodeficiency virus expressing nef of human immunodeficiency virus type 1. *J Virol* **73**, 5814–5825.

Alexander, L., Veazey, R. S., Czajak, S., DeMaria, M., Rosenzweig, M., Lackner, A. A., Desrosiers, R. C. & Sasseville, V. G. (1999b). Recombinant simian immunodeficiency virus expressing green fluorescent protein identifies infected cells in rhesus monkeys. *AIDS Res Hum Retroviruses* **15**, 11–21.

Antoch, G., Stattaus, J., Nemat, A. T., Marnitz, S., Beyer, T., Kuehl, H., Bockisch, A., Debatin, J. F. & Freudenberg, L. S. (2003). Non-small cell lung cancer: dual-modality PET/CT in preoperative staging. *Radiology* **229**, 526–533.

Archibald, S. L., Masliah, E., Fennema-Notestine, C., Marcotte, T. D., Ellis, R. J., McCutchan, J. A., Heaton, R. K., Grant, I., Mallory, M. & other authors (2004). Correlation of *in vivo* neuroimaging abnormalities with postmortem human immunodeficiency virus encephalitis and dendritic loss. *Arch Neurol* **61**, 369–376.

Aylward, E. H., Brettschneider, P. D., McArthur, J. C., Harris, G. J., Schlaepfer, T. E., Henderer, J. D., Barta, P. E., Tien, A. Y. & Pearlson, G. D. (1995). Magnetic resonance imaging measurement of gray matter volume reductions in HIV dementia. *Am J Psychiatry* **152**, 987–994.

Beaumont, M., Odame, I., Babyn, P. S., Vidarsson, L., Kirby-Allen, M. & Cheng, H. L. (2009). Accurate liver T2* measurement of iron overload: a simulations investigation and *in vivo* study. *J Magn Reson Imaging* **30**, 313–320.

Bulte, J. W., Douglas, T., Mann, S., Frankel, R. B., Moskowitz, B. M., Brooks, R. A., Baumgarner, C. D., Vymazal, J., Strub, M. P. &

Frank, J. A. (1994). Magnetoferritin: characterization of a novel superparamagnetic MR contrast agent. *J Magn Reson Imaging* **4**, 497–505.

Cherry, S. R. (2006). Multimodality *in vivo* imaging systems: twice the power or double the trouble? *Annu Rev Biomed Eng* **8**, 35–62.

Choy, G., O'Connor, S., Diehn, F. E., Costouros, N., Alexander, H. R., Choyke, P. & Libutti, S. K. (2003). Comparison of noninvasive fluorescent and bioluminescent small animal optical imaging. *Biotechniques* **35**, 1022–1026.

Chun, T. W., Davey, R. T., Jr, Engel, D., Lane, H. C. & Fauci, A. S. (1999). Re-emergence of HIV after stopping therapy. *Nature* **401**, 874–875.

Chung, J. K. (2002). Sodium iodide symporter: its role in nuclear medicine. *J Nucl Med* **43**, 1188–1200.

Cohen, B., Dafni, H., Meir, G., Harmelin, A. & Neeman, M. (2005). Ferritin as an endogenous MRI reporter for noninvasive imaging of gene expression in C6 glioma tumors. *Neoplasia* **7**, 109–117.

Deans, A. E., Wadghiri, Y. Z., Bernas, L. M., Yu, X., Rutt, B. K. & Turnbull, D. H. (2006). Cellular MRI contrast via coexpression of transferrin receptor and ferritin. *Magn Reson Med* **56**, 51–59.

Di Mascio, M., Paik, C. H., Carrasquillo, J. A., Maeng, J. S., Jang, B. S., Shin, I. S., Srinivasula, S., Byrum, R., Neria, A. & other authors (2009). Noninvasive *in vivo* imaging of CD4 cells in simian-human immunodeficiency virus (SHIV)-infected nonhuman primates. *Blood* **114**, 328–337.

Dothager, R. S., Flentie, K., Moss, B., Pan, M. H., Kesarwala, A. & Piwnica-Worms, D. (2009). Advances in bioluminescence imaging of live animal models. *Curr Opin Biotechnol* **20**, 45–53.

Edinger, M., Cao, Y.-A., Hornig, Y. S., Jenkins, D. E., Verneris, M. R., Bachmann, M. H., Negrin, R. S. & Contag, C. H. (2002). Advancing animal models of neoplasia through *in vivo* bioluminescence imaging. *Eur J Cancer* **38**, 2128–2136.

Eisele, E. & Siliciano, R. F. (2012). Redefining the viral reservoirs that prevent HIV-1 eradication. *Immunity* **37**, 377–388.

Ernst, T., Chang, L., Jovicich, J., Ames, N. & Arnold, S. (2002). Abnormal brain activation on functional MRI in cognitively asymptomatic HIV patients. *Neurology* **59**, 1343–1349.

Evens, N. & Bormans, G. M. (2010). Non-invasive imaging of the type 2 cannabinoid receptor, focus on positron emission tomography. *Curr Top Med Chem* **10**, 1527–1543.

Fletcher, C. V., Staskus, K., Wietgrefe, S. W., Rothenberger, M., Reilly, C., Chipman, J. G., Beilman, G. J., Khoruts, A., Thorkelson, A. & Schmidt, T. E. (2014). Persistent HIV-1 replication is associated with lower antiretroviral drug concentrations in lymphatic tissues. *Proc Natl Acad Sci U S A* **111**, 2307–2312.

Gambhir, S. S., Barrio, J. R., Wu, L., Iyer, M., Namavari, M., Satyamurthy, N., Bauer, E., Parrish, C., MacLaren, D. C. & other authors (2003). Imaging of adenoviral-directed herpes simplex virus type 1 thymidine kinase reporter gene expression in mice with radiolabeled ganciclovir. *J Nucl Med* **39**, 2003–2011.

García, F., Plana, M., Vidal, C., Cruceta, A., O'Brien, W. A., Pantaleo, G., Pumarola, T., Gallart, T., Miró, J. M. & Gatell, J. M. (1999). Dynamics of viral load rebound and immunological changes after stopping effective antiretroviral therapy. *AIDS* **13**, F79–F86.

Genove, G., DeMarco, U., Xu, H., Goins, W. F. & Ahrens, E. T. (2005). A new transgene reporter for *in vivo* magnetic resonance imaging. *Nat Med* **11**, 450–454.

Giavedoni, L. D. & Yilma, T. (1996). Construction and characterization of replication-competent simian immunodeficiency virus vectors that express gamma interferon. *J Virol* **70**, 2247–2251.

Gibbs, J. S., Regier, D. A. & Desrosiers, R. C. (1994). Construction and *in vitro* properties of SIV_{mac} mutants with deletions in 'nonessential' genes. *AIDS Res Hum Retroviruses* **10**, 607–616.

Gottesfeld, Z. & Neeman, M. (1996). Ferritin effect on the transverse relaxation of water: NMR microscopy at 9.4 T. *Magn Reson Med* **35**, 514–520.

Gundlach, B. R., Linhart, H., Dittmer, U., Sopper, S., Reiprich, S., Fuchs, D., Fleckenstein, B., Hunsmann, G., Stahl-Hennig, C. & Uberla, K. (1997). Construction, replication, and immunogenic properties of a simian immunodeficiency virus expressing interleukin-2. *J Virol* **71**, 2225–2232.

Guo, H., Au, W. Y., Cheung, J. S., Kim, D., Jensen, J. H., Khong, P. L., Chan, Q., Chan, K. C., Tosti, C. & other authors (2009). Myocardial T2 quantitation in patients with iron overload at 3 Tesla. *J Magn Reson Imaging* **30**, 394–400.

Guo, Y., Ferdani, R. & Anderson, C. J. (2012). Preparation and biological evaluation of ^{64}Cu labeled Tyr^3-octreotate using a phosphonic acid-based cross-bridged macrocyclic chelator. *Bioconjug Chem* **23**, 1470–1477.

Harrigan, P. R., Whaley, M. & Montaner, J. S. (1999). Rate of HIV-1 RNA rebound upon stopping antiretroviral therapy. *AIDS* **13**, F59–F62.

Hofmann-Lehmann, R., Vlasak, J., Williams, A. L., Chenine, A.-L., McClure, H. M., Anderson, D. C., O'Neil, S. & Ruprecht, R. M. (2003). Live attenuated, *nef*-deleted SIV is pathogenic in most adult macaques after prolonged observation. *AIDS* **17**, 157–166.

Iordanova, B. & Ahrens, E. T. (2012). *In vivo* magnetic resonance imaging of ferritin-based reporter visualizes native neuroblast migration. *Neuroimage* **59**, 1004–1012.

Johnson, W. E. & Desrosiers, R. C. (2002). Viral persistence: HIV's strategies of immune system evasion. *Annu Rev Med* **53**, 499–518.

Judenhofer, M. S., Wehrl, H. F., Newport, D. F., Catana, C., Siegel, S. B., Becker, M., Thielscher, A., Kneilling, M., Lichy, M. P. & other authors (2008). Simultaneous PET-MRI: a new approach for functional and morphological imaging. *Nat Med* **14**, 459–465.

Kemp, B. J., Hruska, C. B., McFarland, A. R., Lenox, M. W. & Lowe, V. J. (2009). NEMA NU 2-2007 performance measurements of the Siemens Inveon preclinical small animal PET system. *Phys Med Biol* **54**, 2359–2376.

Kestier, H. W. III, Ringler, D. J., Mori, K., Panicali, D. L., Sehgal, P. K., Daniel, M. D. & Desrosiers, R. C. (1991). Importance of the *nef* gene for maintenance of high virus loads and for development of AIDS. *Cell* **65**, 651–662.

Kirsch, W., McAuley, G., Holshouser, B., Petersen, F., Ayaz, M., Vinters, H. V., Dickson, C., Haacke, E. M., Britt, W. III & other authors (2009). Serial susceptibility weighted MRI measures brain iron and microbleeds in dementia. *J Alzheimers Dis* **17**, 599–609.

Lecchi, M., Ottobrini, L., Martelli, C., Del Sole, A. & Lucignani, G. (2007). Instrumentation and probes for molecular and cellular imaging. *Q J Nucl Med Mol Imaging* **51**, 111–126.

Logothetis, N. K., Guggenberger, H., Peled, S. & Pauls, J. (1999). Functional imaging of the monkey brain. *Nat Neurosci* **2**, 555–562.

McArthur, J. C. (2004). HIV dementia: an evolving disease. *J Neuroimmunol* **157**, 3–10.

Nader, M. A., Morgan, D., Gage, H. D., Nader, S. H., Calhoun, T. L., Buchheimer, N., Ehrenkaufer, R. & Mach, R. H. (2006). PET imaging of dopamine D2 receptors during chronic cocaine self-administration in monkeys. *Nat Neurosci* **9**, 1050–1056.

Neumann, A. U., Tubiana, R., Calvez, V., Robert, C., Li, T. -S., Agut, H., Autran, B., Katlama, C. & Comet Study Group (1999). HIV-1 rebound during interruption of highly active antiretroviral therapy has no deleterious effect on reinitiated treatment. *AIDS* **13**, 677–683.

Nischang, M., Sutmuller, R., Gers-Huber, G., Audigé, A., Li, D., Rochat, M. A., Baenziger, S., Hofer, U., Schlaepfer, E. & other

authors (2012). Humanized mice recapitulate key features of HIV-1 infection: a novel concept using long-acting anti-retroviral drugs for treating HIV-1. *PLoS One* **7**, e38853.

Patel, Y. C. (1999). Somatostatin and its receptor family. *Front Neuroendocrinol* **20**, 157–198.

Pfefferbaum, A., Adalsteinsson, E., Rohlfing, T. & Sullivan, E. V. (2009). MRI estimates of brain iron concentration in normal aging: comparison of field-dependent (FDRI) and phase (SWI) methods. *Neuroimage* **47**, 493–500.

Pöhlmann, S., Stolte, N., Münch, J., Ten Haaft, P., Heeney, J. L., Stahl-Hennig, C. & Kirchhoff, F. (1999). Co-receptor usage of BOB/GPR15 in addition to CCR5 has no significant effect on replication of simian immunodeficiency virus *in vivo*. *J Infect Dis* **180**, 1494–1502.

Potash, M. J., Chao, W., Bentsman, G., Paris, N., Saini, M., Nitkiewicz, J., Belem, P., Sharer, L., Brooks, A. I. & Volsky, D. J. (2005). A mouse model for study of systemic HIV-1 infection, antiviral immune responses, and neuroinvasiveness. *Proc Natl Acad Sci U S A* **102**, 3760–3765.

Rabinovich, B. A., Ye, Y., Etto, T., Chen, J. Q., Levitsky, H. I., Overwijk, W. W., Cooper, L. J., Gelovani, J. & Hwu, P. (2008). Visualizing fewer than 10 mouse T cells with an enhanced firefly luciferase in immunocompetent mouse models of cancer. *Proc Natl Acad Sci U S A* **105**, 14342–14346.

Sawai, E. T., Khan, I. H., Montbriand, P. M., Peterlin, B. M., Cheng-Mayer, C. & Luciw, P. A. (1996). Activation of PAK by HIV and SIV Nef: importance for AIDS in rhesus macaques. *Curr Biol* **6**, 1519–1527.

Sprague, J. E., Peng, Y., Sun, X., Weisman, G. R., Wong, E. H., Achilefu, S. & Anderson, C. J. (2004). Preparation and biological evaluation of copper-64-labeled Tyr^3-octreotate using a cross-bridged macrocyclic chelator. *Clin Cancer Res* **10**, 8674–8682.

UNAIDS (2013). Global report: UNAIDS report on the global AIDS epidemic 2013. United Nations Joint Programme on HIV/AIDS (UNAIDS). http://www.unaids.org/en/media/unaids/contentassets/documents/epidemiology/2013/gr2013/UNAIDS_Global_Report_2013_en.pdf.

Velikyan, I., Sundin, A., Sörensen, J., Lubberink, M., Sandström, M., Garske-Román, U., Lundqvist, H., Granberg, D. & Eriksson, B. (2014). Quantitative and qualitative intrapatient comparison of ^{68}Ga-DOTATOC and ^{68}Ga-DOTATATE: net uptake rate for accurate quantification. *J Nucl Med* **55**, 204–210.

Venneti, S., Bonneh-Barkay, D., Lopresti, B. J., Bissel, S. J., Wang, G., Mathis, C. A., Piatak, M., Jr, Lifson, J. D., Nyaundi, J. O. & other authors (2008). Longitudinal *in vivo* positron emission tomography imaging of infected and activated brain macrophages in a macaque model of human immunodeficiency virus encephalitis correlates with central and peripheral markers of encephalitis and areas of synaptic degeneration. *Am J Pathol* **172**, 1603–1616.

Vymazal, J., Zak, O., Bulte, J. W., Aisen, P. & Brooks, R. A. (1996). T1 and T2 of ferritin solutions: effect of loading factor. *Magn Reson Med* **36**, 61–65.

Vymazal, J., Brooks, R. A., Bulte, J. W., Gordon, D. & Aisen, P. (1998). Iron uptake by ferritin: NMR relaxometry studies at low iron loads. *J Inorg Biochem* **71**, 153–157.

Wong, J. K., Hezareh, M., Günthard, H. F., Havlir, D. V., Ignacio, C. C., Spina, C. A. & Richman, D. D. (1997). Recovery of replication-competent HIV despite prolonged suppression of plasma viremia. *Science* **278**, 1291–1295.

Yao, B., Li, T. Q., Gelderen, P., Shmueli, K., de Zwart, J. A. & Duyn, J. H. (2009). Susceptibility contrast in high field MRI of human brain as a function of tissue iron content. *Neuroimage* **44**, 1259–1266.

Zhang, X. & Li, C. (2013). Quantitative MRI measures in SIV-infected macaque brains. *J Clin Cell Immunol Suppl* **7**, 005.